IN SILICO ASSEMBLY AND NANOMECHANICAL CHARACTERIZATION OF CARBON NANOTUBE BUCKYPAPER

Steven W. Cranford[1,2], **Markus J. Buehler**[1,2†]

[1]*Laboratory for Atomistic and Molecular Mechanics, Department of Civil and Environmental Engineering, Massachusetts Institute of Technology, 77 Massachusetts Ave. Room 1-235A&B, Cambridge, MA, USA*

[2]*Center for Materials Science and Engineering, Massachusetts Institute of Technology, 77 Massachusetts Ave., Cambridge, MA, USA*

† Corresponding author
Email: mbuehler@MIT.EDU
Phone: +1-617-452-2750
Fax: +1-617-324-4014
Lab URL: http://web.mit.edu/mbuehler/www/

ABSTRACT: Carbon nanotube sheets or films, also known as "buckypaper", have been proposed for use in actuating, structural and filtration systems, based in part on their unique and robust mechanical properties. Computational modelling of such a fibrous nanostructure is hindered by both the random arrangement of the constituent elements, as well as the time and length scales accessible to atomistic-level molecular dynamics modelling. Here we present a novel *in silico* assembly procedure based on a coarse-grain model of carbon nanotubes, used here to attain a representative mesoscopic buckypaper model that circumvents a need for probabilistic approaches. By variation in assembly parameters, including the initial nanotube density and ratio of nanotube type (single- and double-walled), the porosity of the resulting buckypaper can be varied threefold, from approximately 0.3 to 0.9. Further, through simulation of nanoindentation, the Young's modulus is shown to be tunable through manipulation of nanotube type and density over a range of approximately 0.2 to 3.1 GPa, in good agreement with experimental findings of the modulus of assembled carbon nanotube films. In addition to carbon nanotubes, the coarse-grain model and assembly process can be adapted for other fibrous nanostructures such as electrospun polymeric composites, high performance nonwoven ballistic materials, or fibrous protein aggregates, facilitating the development and characterization of novel nanomaterials and composites as well as the analysis of biological materials such as protein fiber films and bulk structures.

Keywords: Carbon nanotubes; buckypaper; fibers; mechanical properties; nanomaterials; assembly; elasticity; modulus; nanomechanics; mesoscale; coarse-grain; porosity; nanoindentation

PACS codes: 31.15.xv, 62.20.de, 62.23.St, 62.25.-g, 81.05.ub, 81.07.De

S. Cranford, M.J. Buehler, " In Silico Assembly and Nanomechanical Characterization of Carbon Nanotube Buckypaper ", Nanotechnology, Vol. 21, paper # 265706, 201

1. INTRODUCTION

Carbon nanotubes (CNTs) and related materials are amongst the most widely studied nanomaterials, with many potential applications that take advantage of their unique mechanical, electrical, thermal, and optical properties [1]. The superior mechanical properties of carbon nanotubes are appealing for their potential use in novel nanomaterials. For instance, the Young's modulus of a single-walled nanotube approaches a terapascal (10^{12} Pa) [2], implying that CNT is one of the strongest known synthesized materials in terms of both its elastic modulus and its ultimate tensile strength [3]. For over a decade, attempts have been made to utilize the high strength of individual CNTs in an efficient manner, and in particular at larger length-scales.

Nanotube sheets, films, or membranes have been proposed for use in actuating, structural, filtration, and electrochemical systems, based in part on their unique and robust mechanical properties. In addition, the range of carbon nanotube properties as a function of type (single- or multi-walled) and size (total length, diameter) [4], chirality [5], and purity [6] allows control of composite nanotube behavior. For example, the use of relatively stiff (large diameter) and long multi-walled CNTs results in stiffer, more porous films [7], whereas the use of fine, smaller diameter, short tubes results in a dense tube network, suitable for use in polymer composites [8]. The choice of the types of CNT extends the potential design space, resulting in tunable material behavior derived from similar constituent components. However, fabricating macroscopic structures, which have controlled geometries, porosity and mechanical properties, is a promising yet challenging endeavor. Supplementary to empirical and synthesis efforts, computational approaches can provide a means to investigate potential carbon nanotube structures, indicating possible systems and configurations that warrant experimental and physical realization.

The molecular level interactions of adjacent carbon nanotubes has been investigated using atomistic methods [9-13], but systems consisting of complex CNT components (such as arrays and films) become computationally expensive at the atomistic level for relatively long carbon nanotubes, or when multiple nanotubes are involved (as the computational cost is proportional to the number of atoms in the simulation). Furthermore, the particular type of intermolecular interactions between carbon nanotubes (weak dispersive interactions) and the nanoscale dimensions of this material in ranges from a few nanometers to hundreds of nanometers and micrometers require the development of coarse-grain mesoscale models beyond the capacity of traditional continuum and structural mechanics. Mesoscopic

"bead-spring" methods have been proven a viable approach to simulate arrays of CNTs [14-16] as well as graphene assemblies [17]. The intent of the model developed and applied here is to extend the time- and length-scales accessible to atomistic simulations to enable the simulation of large-scale multi-nanotube structures. Additionally, the model reported here could potentially be parameterized to provide an efficient means to investigate the mechanical properties of similar fibrous systems at both meso- and micro-scales, such as fiber materials and nanoscale fabrics (Figure 1).

The propensity of carbon nanotubes to adhere in bundles results in the formation of stable films via the deposition of suspended nanotubes in solution on a suitable substrate. The result is a self-entangled and agglomerated aggregate of nanotubes. The CNTs are randomly arranged into a non-woven fibrous structure resulting in a highly porous 3D network with large specific surface area. The term "buckypaper" (a portmanteau of buckminsterfullerene and paper) is used to describe such a mat of randomly entangled CNTs and is used hereafter to refer to such carbon nanotube films. The production of buckypaper is one of the simplest and most efficient means of processing carbon nanotubes at large scales; where synthesized carbon nanotubes are dispersed in an aqueous solution, the suspension is membrane filtered, and the result is a deposited uniform film. As such, it provides a promising framework for large-scale nanotube applications. Buckypaper is being investigated for multiple applications, including thermal and electrical conductive materials, catalysts, filtration and distillation membranes, and actuators, exploiting the intrinsic and robust properties of the constituent carbon nanotubes [8, 17-23]. Despite these numerous applications, there currently exists few models that provide an accurate account of the material properties from the bottom up, a key issue in tuning the properties of buckypaper for engineering applications.

Here, we address this issue and focus on the bottom-up development of a mesoscopic fiber model, parameterized to represent carbon nanotube based buckypaper. We then proceed to apply our model to characterize the mechanical properties of buckypaper, specifically in terms of porosity and mechanical stiffness, illustrating potential control and tunability of each property based on nanostructural variation. The outline of this paper is as follows: In Section 2, the computation method to construct the mesoscopic buckypaper model will be described. Section 2.1 focuses on the employed coarse-grain nanotube nanotube representation, while Section 2.2 describe the assembly procedure to arrive at the buckypaper model configuration. Section 3 encompasses the nanomechanical characterization of the buckypaper, including porosity (Section 3.1) and contact stiffness and Young's modulus through

nanoindentation (Section 3.2). The results and implications of the modeling results are concluded in Section 4.

2. MESOSCALE REPRESENTATION AND MODEL ASSEMBLY

The prevalence of intermolecular interactions and their complex geometry hinders a continuum representation of buckypaper, while the scale and number of nanotubes prevents efficient molecular modeling at the atomistic scale. Consequently, such material systems require multi-scale methods to model and investigate nanostructures and mechanical behavior at scales from nanometers to micrometers that fall precariously between atomistic and continuum techniques. Here, we utilize a coarse-grain mesoscopic representation of the constituent nanotubes and implement a novel *in silico* assembly procedure to arrive at a representation of deposited carbon nanotube films.

2.1 Carbon Nanotube Coarse-Grain Representation

For the carbon nanotubes, a "fine-trains-coarse" multi-scale approach is implemented to produce mesoscale model derived solely from atomistic calculations [14-16]. A series of full atomistic calculations of mechanical test cases (test suite) is implemented via classical molecular dynamics (MD) to derive a simplified set of parameters to describe the nanotube behavior. The full atomistic model utilizes a reactive force field (ReaxFF) [24, 25] potential for the behavior of nanotubes implemented via the massively paralyzed MD modeling code LAMMPS (http://lammps.sandia.gov/) [26]. The test suite consists of the following three loading cases: (i) tensile loading, to determine Young's modulus; (ii) bending to determine the bending stiffness of CNTs; and (iii) an assembly of two CNTs to determine the adhesion energy. For a more detailed description of the atomistic simulations and results, the reader is referred to references [14] and [16]. Here we provide only a brief review of the multi-scale approach. Figure 2(a) depicts the molecular model of a (5,5) single-walled nanotube as an example.

The method in deriving parameters for a mesoscale bead-type model of CNTs from the full atomistic calculation is based on a principle of energy conservation between full atomistic and coarse-grain potentials. The mesocale model is represented by a function of the total energy of the system expressed as

$$E_{\text{System}} = E_{\text{T}} + E_{\text{B}} + E_{\text{pairs}} = \sum_{bonds} \phi_{\text{t}}(r) + \sum_{angles} \phi_{\theta}(\theta) + \sum_{pairs} \phi_{\text{LJ}}(r), \quad (1)$$

where E_{T} is the energy stored in the chemical bonds due to axial stretching, E_{B} is the energy due to bending, and E_{pairs} is the energy due to weak interactions. The total energy contribution of each is calculated by a sum over all pair-wise (distance) and triple (angular) interactions in the system. The contributions are summarized as follows for brevity:

i) Axial Stiffness: From the full atomistic results, the axial stretching behavior of carbon nanotubes is determined. We can calculate the effective Young's modulus directly via force-displacement results from the full atomistic simulation. Nonlinear behavior is neglected, as the coarse-grain simulations will be limited to small deformation conditions. The total bond energy of the coarse-grain system is given by the sum over all bonded interactions (Eq. (1)). For axial stretching a simple harmonic spring is used to determine the energy between all bonded pairs of particles in the system, given by:

$$\phi_{\text{t}}(r) = \frac{1}{2} k_{\text{t}} (r - r_0)^2, \quad (2)$$

with k_{t} as the spring constant relating distance, r, between two particles relative to the equilibrium distance, r_0. We assume each linear regime can be approximated using the equivalent elastic strain energy and utilize the determined Young's modulus from full atomistic simulations to allow the formulation of strain energy and an equivalent k_{t}.

ii) Bending Stiffness: For the angle potential, E_{B}, the bending stiffness and force-displacement behavior of each structure is required. A simple three-point bending test is simulated via full atomistic representation, with the macromolecule subjected to bending by a center point load. From the results, we can determine the bending stiffness of the molecule, which we label *EI*. The bending energy is given by a sum over all triples in the system (Eq. (1)). For bending a rotational harmonic spring potential is used to determine the energy between all triples of particles in the system:

$$\phi_{\theta}(\theta) = \frac{1}{2} k_{\theta} (\theta - \theta_0)^2, \quad (3)$$

with k_θ as the spring constant relating bending angle, θ, between three particles relative to the equilibrium angle, $\theta_0 = 180°$. Again, using the equivalent elastic energy, we utilize the bending stiffness, *EI*, from full atomistic simulations to allow the formulation of elastic energy and an equivalent k_θ.

iii) Adhesion Energy: We next characterize weak interactions (van der Waals interactions) between all pairs of non-bonded coarse-grain elements, E_{pairs}. The weak interactions represent the adhesion between adjacent macromolecules, thus a full atomistic simulation with two molecules is simulated to determine the adhesion energy. The energy barrier and equilibrium distance can be quickly determined by minimizing the atomistic system. Differences in energy minima can be used to extract potential energy gain of adhesion per unit length, while the geometric configuration at contact can be used to determine equilibrium distances. Here we assume a Lennard-Jones 12:6 function to represent adhesion, requiring the potential energy well depth and equilibrium distance:

$$\phi_{\text{LJ}}(r) = 4\varepsilon \left[\left(\frac{\sigma}{r} \right)^{12} - \left(\frac{\sigma}{r} \right)^{6} \right], \quad (4)$$

where ε describes the energy well depth at equilibrium, and σ is the distance parameter. We assume that a pair-wise interaction between different particles is sufficient to describe the adhesion between the coarse-grain elements.

The “fine-trains-coarse” approach eliminates the reliance on empirical parameter tuning. From atomistic simulations using scales of femtoseconds and Angstroms, a set of mesoscopic parameters was derived as outlined above. The resulting mesoscale model enables modeling of the dynamics of systems with hundreds of ultra long CNTs over time scales approaching microseconds, facilitating a bridge between atomistic theory and simulation of actual physical experiments. The mesoscopic model for carbon nanotubes can be defined by six parameters: k_t; r_0; k_θ; θ_0; σ, and; ε. The results from the above atomistic simulations are used to determine the parameters via equilibrium conditions (r_0; θ_0; σ)

and energy conservation (k_t; k_θ; ε). Figure 2(b) depicts the coarse-grain bead-spring model of the nanotube. The above "test suite" is applied both (5,5) single wall carbon nanotubes (SWCNTs) and (8,8)-(12,12) double-walled carbon nanotubes (DWCNTs) to allow the implementation of both SWCNT and DWCNT representations in the mesoscopic model. We note that the choice of these specific nanotube structures and chiralities is motivated by their successful use in previous investigations [14-16]. As buckypaper can potentially be fabricated with many possible synthesized CNT structures, it is considered appropriate to utilize the models the authors have previously developed. Moreover, the presented assembly procedure can easily be adapted to other geometries of CNTs and fibrous structures, and the current configuration can be considered a model system for future extended applications. All coarse-grain parameters are given in Table 1. Because of the use of a multi-scale approach, the atomistic behavior and intramolecular interactions are maintained, thereby providing a necessary intermediate step reconciling the gap between atomistic and continuum theory.

2.2 Buckypaper Assembly – *In silico* Deposition

The randomness of fibrous networks as found for example in buckypaper is a challenge to modeling, as any such simulation requires the knowledge of the initial geometry. Different approaches to generate a representative structure have been proposed. Such methods include random beam networks as utilized in finite element analysis [27], random perturbations from a regular initial configuration [28], Boolean models parameterized with empirical morphological data [29], or the use of Delaunay triangulation to generate random fiber junction distributions [30]. For the application to buckypaper it is evidently desirable to create a representation of the material that is inherently stochastic. Here, we circumvent the generation of a "pseudo-random" network by developing an *in silico* assembly procedure that does not require a sophisticated probabilistic framework for structure formulation but rather relies on the direct simulation of the assembly process.

To replicate an entangled network of carbon nanotubes, a simulated assembly procedure is motivated by the physical process of buckypaper production. The physical synthesis of buckypaper *in situ* can be summarized as follows: a purified admixture of CNTs is dispersed in a suitable solvent with the concentration and type of nanotubes being controlled variables. Once a well-dispersed solution is achieved, it is filtered through a porous medium, which captures the CNTs while allowing the solution to permeate (through vacuum filtration), creating a deposited film of entangled nanotubes, randomly

oriented yet predominately in plane with the film [7, 31]. The details of the purification and dispersion techniques are critical to the final buckypaper structure and properties.

The simulated assembly as pursued here attempts to take advantage of such a deposition process. First, a “reservoir” of carbon nanotubes is generated, consisting of regular layers of aligned tubes in-plane. For the current investigation, twelve layers are generated, consisting of ten individual nanotubes (120 nanotubes total), and the tubes are of constant length (50 nm). Each layer is rotated thirty degrees about a central axis, such that 12 layers represent a complete 360° period of initial tube orientation. A rotation of 30° is introduced to facilitate CNT entanglement and to approximate in-plane isotropy of the resulting buckypaper representation. It has been shown that the alignment and orientation of nanotubes constituting buckypaper can affect their thermal/electrical properties [18] as well as the mechanical behavior [32, 33] of the buckypaper system. However, such systems would not benefit from the assembly procedure developed here specifically for randomly entangled structures. It also behooves us to note that the current mesoscale model presumes “perfect” constituent nanotubes, that is, without impurities or defects (an issue that could be easily changed in future studies). The reservoir configuration is reflective of the pre-processing of the physical nanotube dispersion, and here variations could be introduced, including variation in nanotube length distribution, nanotube type (single-, double-, or multi-walled), defects, and alignment.

The assembly procedure consists of a stepwise deposition of nanotube layers onto a substrate, representing the porous medium implemented in vacuum filtration. An NVT ensemble is used with a constant temperature of 300K, a small viscous damping force to simulate the frictional damping of solution (approximately 10 μN/m-s^{-1}), and an integration timestep of 50 femtoseconds. A single layer is released from the reservoir, while the remaining layers are fixed. The free layer is allowed to equilibrate for 5,000 timesteps, then subject to a body force directed towards the substrate (representing the pressure due to vacuum filtration). The nanotube adhesion to a substrate is modeled by interaction with a Lennard-Jones (LJ) wall. The substrate is simply represented by an effective LJ 9:3 potential at a designated *xy*-plane, where:

$$\phi_{\text{wall}}\left(z_i\right) = \varepsilon_{\text{wall}}\left[\frac{2}{15}\left(\frac{\sigma_{\text{wall}}}{z_i}\right)^9 - \left(\frac{\sigma_{\text{wall}}}{z_i}\right)^3\right], \tag{5}$$

with σ_{wall} representing the effective minimum normal distance between the wall and a particles and ε_{wall} the strength of substrate interaction. The Lennard-Jones 9:3 interaction is derived by integrating over a half-lattice of Lennard-Jones 12:6 particles, effectively representing a homogeneous substrate of arbitrary thickness. Since it is not straightforward to directly link this strength of adsorption to experimental values, we choose parameters so as to mimic good "anchoring" properties to the planar surface. Test cases indicate that deviations in the selected parameters (ε_{wall} and σ_{wall}) have a limited affect on the assembled structures. We refer to the LJ wall as the "substrate" in the following discussion. Once a layer reaches the adhesion plane, the nanotubes are again allowed to equilibrate for 50,000 timesteps (2.5 nanoseconds), after which the succeeding layer is released from the reservoir (See Figure 3 for a schematic of the assembly procedure).

Reaching CNT entanglement is facilitated by the manipulation of coarse-grain parameters. During the assembly process, the variables for the bending stiffness (k_θ) as well as tube interactions (ε) are reduced significantly. The purpose is twofold: The bending stiffness reduction essentially converts the rigid nanotube to a more flexible fiber by decreasing the intrinsic persistence length. The thermal energy of the mesoscopic system, combined with the flexibility of the tubes, results in the "mixing" of nanotubes, encouraging overlaps, misalignment, and disorder on the substrate within each deposited layer. The reduction in the Lennard-Jones parameter, ε, provides an upper limit to the intertube forces that typically result in nanotube adhesion and regular bundle formation. By decreasing this force, the tubes can subsequently "pass through" each other, due to the bead-spring representation, via a "stick-slip" mechanism through the overlapping LJ pair interactions. Through manipulation of the inter-tube adhesion, subsequent deposited layers are ultimately entangled, as some segments of the nanotubes penetrate preceding deposited layers. Combined with the disarray within each layer due to the reduction in stiffness, the end result is randomly entangled agglomerate of carbon nanotubes. It is noted that, by allowing individual tubes to "slip" through another, the deposition process is not meant to emulate the physical assembly procedure, but rather utilized as a means to attain a representative and entangled material nanostructure.

The final step is to return the reduced parameters (k_θ and ε) to the initial values (those given in Table 1), as well as to remove the constraint of the substrate to result in a freestanding nanotube structure. The assembled nanotube structure is then subjected to system relaxation and equilibration (approximately 5 nanoseconds, or 100,000 timesteps). The final structure is then used as the initial

structure of mechanical testing and characterization, bypassing the need for assembly each simulation (See Figure 4(a) for a representative model).

3. NANOMECHANICAL CHARACTERIZATION

As stated, buckypaper and other CNT-based materials are promising due to the inherent mechanical strength and chemical stability of carbon nanotubes. Additionally, the intrinsic porosity and relatively high surface area of nanotube films stimulates the potential for filtration applications (where pores allow permeability) or in advanced composite materials (where pores and surface area facilitate interfacial bonding). Here we investigate the variability of both porosity and stiffness, which are critical parameters in prospective buckypaper applications, using the computational model described above.

3.1 Porosity

Due to the entangled aggregation process of assembly, nanotube films do not consist of well-defined pores of a single characteristic shape and size. However, control over the pore structure is a prerequisite for applications that exploit the high-porosity and mechanical strength inherent to buckypaper. Techniques to measure porosity empirically include SEM imaging, relative density measurements, and comparative perfusion rates (see [7] and the citations therein). Here the mesoscale model allows direct measurement of nanotube density within the buckypaper aggregate. We determine the porosity of the assembled buckypaper by considering a representative volumetric element (RVE) from the bulk of the model (Figure 4(b)), where the porosity is defined as:

$$\Omega = \frac{V_{\text{voids}}}{V_{\text{RVE}}} = 1 - \frac{V_{\text{CNT}}}{V_{\text{RVE}}}, \tag{6}$$

where V_{RVE} is the volume of the RVE (constant) and V_{CNT} is the volume of the carbon nanotubes contained within the RVE. The total volume of the nanotubes is calculated by a summation of the total length and effective cross-section areas of the tubes. The effective cross-sectional area assumes an effective diameter by the addition of the carbon nanotube width (d_{CNT}) plus the van der Waals spacing between adjacent tubes (d_{vdW}; approximately 3.7 Å) (see Figure 5 for schematic).

The porosity of buckypaper *in situ* can be manipulated through multiple experimental techniques, including combinations of nanotubes of different diameters [7], controlled alignment of the nanotubes [18], variation in the length of constituent nanotubes [34], as well as the addition of polymers [35]. Here, we control the porosity via two methods. First, we exploit the initial carbon nanotube spacing in the reservoir to manipulate the density of deposited nanotubes. During the assembly process, the nanotube distribution of sequential layers remains constant, thus tightly packed nanotubes result in relatively low porosity, while larger spacing results in higher porosity. The entanglement of nanotubes prevents the formation of large aligned nanotube bundles. Second, we manipulate the content of DWCNTs. The addition of the larger diameter nanotubes results in a decrease in porosity.

For buckypaper consisting of only SWCNTs, the initial spacing is varied during deposition from 10 Å to 100 Å, while the number of nanotubes and deposited layers remains constant. The same RVE is considered for each assembled buckypaper model, and the porosity is calculated as described by Eq. (6). The variation in porosity ranges from approximately 0.47 to 0.90 (See Figure 6). A summary of results is found in Table 2(a). We note that an initial spacing of 10 Å is relatively dense, as the tubes are approximately at equilibrium spacing, thus the porosity value of 0.47 represents a lower-bound for the current type of SWCNT used in the making of the buckypaper material. For initial spacings of 50 to 100 Å, the porosity falls within a range of 0.77 to 0.90. Such values are in agreement with experimental data, where measurements made on fabricated buckypaper indicate porosities on the order of approximately 0.80 to 0.90 [7, 23, 36]. The introduction of DWCNTs provides additional control of attained porosity, with the larger diameter tubes resulting in relatively smaller voids. DWCNT content by weight is varied from 0% to 50%, from an initial spacing of 10 Å for comparison (Figure 6). After relaxation and equilibration, the resulting porosities range from 0.28 to 0.47 (See Table 2(b)). Physically, the initial nanotube spacing and DWCNT content in the reservoir is reflective of the pre-processing of the carbon nanotube dispersion, and current model parameters can be tuned to attain experimental results as required, and also provide a reciprocal means to predict porosity from experimental conditions.

The relatively high and variable porosity of fabricated buckypaper naturally leads to potential applications as tunable permeable films, including membrane distillation [23], biogas purification [37], and antimicrobial filtration of bacteria and viruses (such as *E. coli*) [22, 38, 39]. We note that the range

of attainable pore sizes and relatively simple fabrication in combination with the mechanical and thermal stability of carbon nanotubes motivates the development of such “buckypaper filters”.

3.2 Computational Nanoindentation

Nanoindentation tests are one of the most commonly applied means of physically testing the mechanical properties of small volumes of materials. Such tests result in the direct determination of material parameters such as material hardness and modulus of elasticity. The indentation process itself is simple; where an indenter tip is pressed into the material and the force-penetration relationship is recorded. The relatively straightforward procedure can be replicated via simulation. The simulation of a nanoindentation at the mesoscale level is beneficial for a multitude of reasons. Primarily, such investigations can be linked to actual physical experiments (see [40] for an example of buckypaper nanoindentation), providing a critical connection between empirical results and theoretical basis. Further, the simulation technique can be used as parametric study to investigate the behavior of a material efficiently prior to physical empirical verification.

The mesocopic simulation of nanoindentation does not require the presence of a physical indenter (e.g. a collection of atoms/beads is not required). Rather, the indentation experiment is simulated by the introduction an indenter force field within the simulation box. A harmonic spherical indenter is used, which exerts a force of magnitude:

$$F(r_i) = K(r_i - R)^2, \qquad (7)$$

where K is the specified force constant, r_i is the distance from the atom to the center of the indenter, R is the radius of the indenter. Both the force and position of the indenter tip are recorded during the simulation, resulting in the desired force-penetration relationship. Figure 7 shows a schematic of the indenter on the buckypaper. We use an indenter radius of 25 nm, a force constant approximately 10 N/m, and an indentation speed of 30 m/s. Due to the use of harmonic potentials in the formulation of the bead-spring representation of the nanotubes, indentation is not carried out until yielding, but rather to depth of only 2.0 nm, ensuring a small deformation regime. An analytical model for contact between a rigid indenter of defined shape can be used to model the contact stiffness [41]:

$$S = \frac{2\sqrt{A}}{\sqrt{\pi}} E_{\mathrm{r}}, \tag{8}$$

where S is the contact stiffness (N/m), A is the contact area (m^2), and E_{r} is the reduced modulus (N/m^2). The contact area is calculated using the portion of the surface area of the spherical indenter (with radius R) at the maximum penetration depth, $h_{\max}$, where:

$$A = 2\pi R h_{\max}. \tag{9}$$

The relationship assumes a homogenous isotropic elastic material, which is not the case for the current model. However, more sophisticated methods of determining the contact stiffness of buckypaper is considered superfluous to the current investigation and the above relationship is deemed a suitable approximation for small deformation. Combining the target sample and the indenter as a series of springs, the reduced modulus can also be represented by:

$$\frac{1}{E_{\mathrm{r}}} = \left(\frac{1-\nu^2}{E}\right)_{\mathrm{indentor}} + \left(\frac{1-\nu^2}{E}\right)_{\mathrm{sample}}. \tag{10a}$$

As the indenter is not modeled as a physical material (*i.e.* it undergoes zero deformation), it is assumed that $E_{\mathrm{indent}} >> E_{\mathrm{sample}}$. Further, if the Poisson's ratio is small (see [42]), the above relationship is simplified to:

$$\frac{1}{E_{\mathrm{r}}} = \frac{1}{E_{\mathrm{sample}}} \rightarrow E_{\mathrm{r}} = E_{\mathrm{sample}}. \tag{10b}$$

Due to the heterogeneity of the surface of the buckypaper, each investigated configuration is subject to four nanoindentation simulations, where the location of indentation is perturbed about the center of the model (indentation axis randomly offset by Δ in both the *x*- and *y*-directions where $\Delta \in$ [-20, 20] Å). Single simulated nanoindentation results can contain significant fluctuations in the force-indentation behavior due to local slipping of individual nanotubes subject to indentation force (see for example, Figure 8). For example, for the individual indentation results shown, the calculated contact stiffness

ranges from 17.1 N/m to 29.8 N/m, with a standard deviation of 6.1 N/m. To account for fluctuations, the average indentation force versus depth is calculated, and the contact stiffness is determined by fitting a linear regression to the average over a range of 0.5 nm to 1.5 nm penetration (see Figure 8 for representative results), from which the modulus is calculated by Eq. (8) through Eq. (10).

Eight distinct configurations, through manipulation of initial spacing and DWCNT content, are investigated, resulting in a modulus ranging from 0.22 GPa for SWCNT with a relatively high porosity to 3.14 GPa for high DWCNT content with relatively low porosity. Figure 9 depicts the average indentation force versus depth for SWCNT only configurations of representative porosities 0.473, 0.771, and 0.902 while Figure 10 depicts the results for DWCNT contents of 0%, 16%, and 50% (porosities of 0.473, 0.427, and 0.283, respectively). The results of all nanoindentation simulations are summarized in Table 3. To investigate the possible effect of layer orientation angle, as a case study, we prepared a 10-layer model with 45° rotation between nanotube layers. The 10-layer model was still thick enough to allow the same RVE selection. We implement an all (5,5) SWCNT configuration, with initial spacing of 10 Å. After assembly, again both porosity and indentation characterization are carried out. The porosity is determined to be ≈ 0.71, which is a substantial increase from $\Omega = 0.473$ obtained using 30° orientations under the same assembly conditions. Subsequent indentation characterization result in a contact stiffness of 20.6 N/m and a modulus of 1.2 GPa. This result agrees quantitatively with the general trend of modulus versus porosity given in Figure 11. Although mechanical responses may change significantly with manipulation of orientation (*i.e.* highly aligned structures), limited changes in layer assembly rotations have resulted in similar system behavior.

We consider the change in modulus for both cases - variation in porosity due to initial nanotube density (SWCNT spacing) and variation in DWCNT content – as a direct comparison of the change in modulus between is inappropriate. For both sets of results, the modulus changes approximately linearly with respect to porosity (see Figure 11). In the first case (SWCNT only), the change can be attributed to the amount of material in contact with the indenter, as an increase in porosity results in less nanotubes to provide resistance. For the second case (SWCNT plus DWCNT), an increase in porosity is not due to an increase in nanotubes, but rather due to an increase in larger diameter (and innately stiffer) DWCNTs, thus causing an increase in modulus at a significantly greater rate. By manipulating the DWCNT content and initial nanotube density, the modulus can effectively be “tuned” within the range of the results shown.

The resulting range of moduli is around the same order of magnitude as reported experimentally for "pristine" single-walled nanotube sheets of approximately 1.1 GPa to 4 GPa [27, 43] (depending on the method of synthesis). However, it behoves us to note that these reported moduli implement nanotubes with diameters and mechanical properties that differ from the present model. The illustrated range of attainable moduli and stiffness introduces a promising design parameter for similar fiber- or nanotube-based materials [44]. The inherent porosity of buckypaper could provide a unique scaffold for the synthesis of advanced polymer-nanotube composites (see [8] for example) with "tunable" mechanical properties derived from the synthesis of the same constituent components.

4. CONCLUSIONS

We have shown here that variations in nanostructural and mechanical properties of entangled fibrous systems can be achieved during assembly with minimal effort through manipulation of both the nanotube type and the density. This finding is the most important result of the case studies put forth in this article, which illustrates the potential control of a material system, introducing assembly procedures resulting in tunable mechanical properties with designed intent. Other important contributions of this paper include the development of a novel, *in silico* assembly procedure to produce entangled fibrous nanostructures as well as an efficient means of predictive simulation to investigate system configurations and properties prior to physical synthesis. The approach developed here could be used for many other fibrous material systems, such as polymer based materials and protein materials.

The specific types of intermolecular interactions between carbon nanotubes at the nanoscale, combined with the randomness of such fibrous networks at larger (meso)-scales necessitate new approaches to model such systems. Here we implemented a coarse-grain model to investigate aggregations of carbon nanotubes.. The entanglement and disorder of buckypaper complicates the formation of representative models, which typically implement probabilistic measures to obtain random fibrous structures. We provide an alternate procedure, motivated by the physical synthesis of buckypaper, whereby the nanotubes are assembled via *in silico* deposition. By careful manipulation of the model parameters, the deposition is driven by the intrinsic stochastic dynamics of the simulation, resulting in a representative structure of entangled nanotubes. Further, we showed that a range of porosity values can be obtained via manipulation of initial assembly conditions, indicating promising extension to other nanotube and fibrous systems beyond the scope of the current investigation. Relatively high levels of porosity,

combined with inherent mechanical strength and structural stability motivate potential for filtration, selective membrane, and chemical separation applications.

In addition to computational investigations, mesoscopic models can also provide support to concurrent experimental investigations by extending the time- and length-scales of nanoscopic materials to physical regimes (e.g. systems of carbon nanotubes rather than individual tubes or small bundles). Indeed, the incentive for simulating physical investigative methods, such as nanoindentation, is twofold: (1) to supply validity to the representative model, by allowing a direct comparison of theoretical and empirical results, and (2) providing an efficient means of investigating multiple system parameters prior to physical realization. Here, through nanoindentation results, the determined Young's modulus of the assembled buckypaper correlates well with values determined experimentally. Moreover, the resulting structural model can be easily manipulated to attain a desired modulus throughout the resulting range. Such modeling can be implemented to provide a predictive nanoengineering tool for designed buckypaper or other fibrous structures, while delineating the upper and lower bounds of achievable moduli or other mechanical properties, allowing tunable design parameters using the same universal material components. As demonstrated, the current mesoscopic model provides a predictive tool to investigate various mixtures of carbon nanotubes, and could potentially be extended to show the effect of nanotube-polymer composites [8], or chemical functionalization [45] through the implementation of additional or more complex coarse-grain potentials and interactions. Further, similar models and assembly procedures could be exploited for other nano- and mesofiber aggregate systems including synthetic materials such as electrospun polymer composites [46-48] or biological materials such as amyloid protein films [49]. With coarse-grain approaches, more complex microscale systems can be investigated, with a solid theoretical foundation in atomistic behavior and molecular mechanics, facilitating the development of novel nanoscale materials and applications.

5. ACKNOWLEDGMENTS

This work was supported primarily by the MRSEC Program of the National Science Foundation under award number DMR-0819762. The calculations and the analysis were carried out using a parallelized LINUX cluster at MIT's Atomistic Mechanics Modeling Laboratory. Visualization has been carried out using the VMD visualization package [50].

6. REFERENCES

1. Baughman, R.H., A.A. Zakhidov, and W.A. de Heer, *Carbon Nanotubes - the Route Toward Applications.* Science, 2002. **297**: p. 787-792.
2. Treacy, M.M.J., T.W. Ebbesen, and J.M. Gibson, *Exceptionally high Young's modulus observed for individual carbon nanotubes.* Nature, 1996. **381**: p. 678-680.
3. Li, F., et al., *Tensile strength of single-walled carbon nanotubes directly measured from their macroscopic ropes.* Applied Physics Letters, 2000. **77**(20): p. 3161-3163.
4. Ruoff, R., D. Qian, and W.K. Liu, *Mechanical properties of carbon nanotubes: theoretical predictions and experimental measurements.* C. R. Physique, 2003. **4**: p. 993–1008.
5. Mori, H., et al., *Chirality dependence of mechanical properties of single-walled carbon nanotubes under axial tensile strain.* Japanese Journal of Applied Physics Part 2-Letters & Express Letters, 2005. **44**(42-45): p. L1307-L1309.
6. Salvetat, J.P., et al., *Mechanical properties of carbon nanotubes.* Applied Physics a-Materials Science & Processing, 1999. **69**(3): p. 255-260.
7. Sears, K., et al., *Recent Developments in Carbon Nanotube Membranes for Water Purification and Gas Separation.* Materials, 2010. **3**(1): p. 127-149.
8. Pham, G.T., et al., *Mechanical and electrical properties of polycarbonate nanotube buckypaper composite sheets.* Nanotechnology, 2008. **19**(32): p. 325705.
9. Chen, B., et al., *Binding energy of parallel carbon nanotubes.* Applied Physics Letters, 2003. **83**(17): p. 3570 - 3571
10. Liew, K.M., C.H. Wong, and M.J. Tan, *Tensile and compressive properties of carbon nanotube bundles.* Acta Materialia, 2006. **54**: p. 225-231.
11. Liew, K.M., C.H. Wong, and M.J. Tan, *Buckling properties of carbon nanotube bundles.* Applied Physics Letters, 2005. **87**(041901).
12. Zhou, W., et al., *Self-folding of single- and multiwall carbon nanotubes.* Applied Physics Letters, 2007. **90**(073107).
13. Zhu, C., Z. Xie, and K. Guo, *Formation of close-packed multi-wall carbon nanotube bundles.* Diamond and Related Materials, 2004. **13**(1): p. 180-183.
14. Buehler, M.J., *Mesoscale modeling of mechanics of carbon nanotubes: self-assembly, self-folding, and fracture.* Journal of Materials Research, 2006. **21**(11): p. 2855-2869.
15. Cranford, S. and M.J. Buehler, *Mechanomutable carbon nanotube arrays.* International Journal of Materials and Structural Integrity, 2009. **3**(2/3): p. 161-178.
16. Cranford, S., et al., *A single degree of freedom 'lollipop' model for carbon nanotube bundle formation.* Journal of the Mechanics and Physics of Solids, 2009. **58**(3): p. 409-427
17. Cranford, S., D. Sen, and M.J. Buehler, *Meso-origami: Folding multilayer graphene sheets.* Applied Physics Letters, 2009. **95**(123121).
18. Wang, D., et al., *Highly oriented carbon nanotube papers made of aligned carbon nanotubes.* Nanotechnology, 2008. **19**(7): p. 075609 (6pp)
19. Park, J.G., et al., *The high current-carrying capacity of various carbon nanotube-based buckypapers.* Nanotechnology, 2008. **19**(18): p. 185710.
20. Suppiger, D., S. Busato, and P. Ermanni, *Characterization of single-walled carbon nanotube mats and their performance as electromechanical actuators.* Carbon, 2008. **46**(7): p. 1085-1090.
21. Zhu, W., et al., *Durability Study on SWNT/Nanofiber Buckypaper Catalyst Support for PEMFCs.* Journal of the Electrochemical Society, 2009. **156**(9): p. B1099-B1105.
22. Brady-Estevez, A.S., S. Kang, and M. Elimelech, *A single-walled-carbon-nanotube filter for removal of viral and bacterial pathogens.* Small, 2008. **4**(4): p. 481-484.

23. Dumee, L., et al., *Characterization and evaluation of carbon nanotube Bucky-Paper membranes for direct contact membrane distillation.* Journal of Membrane Science, 2010. **351**(1): p. 36-43.
24. Chenoweth, K., A.C.T. van Duin, and W.A. Goddard, *ReaxFF reactive force field for molecular dynamics simulations of hydrocarbon oxidation.* Journal of Physical Chemistry A, 2008. **112**(5): p. 1040-1053.
25. van Duin, A.C.T., et al., *ReaxFF: A reactive force field for hydrocarbons.* Journal of Physical Chemistry A, 2001. **105**(41): p. 9396-9409.
26. Plimpton, S.J., *Fast parallel algorithms for short-range molecular dynamics.* Journal of Computational Physics, 1995. **117**: p. 1-19.
27. Berhan, L., et al., *Mechanical properties of nanotube sheets: Alterations in joint morphology and achievable moduli in manufacturable materials.* Journal of Applied Physics, 2004. **95**(8): p. 4335-4345.
28. Silling, S.A. and F. Bobaru, *Peridynamic Modeling of Membranes and Fibers.* International Journal of Non-Linear Mechanics, 2005. **40**(2-3): p. 395-409.
29. Peyrega, C., et al., *3d Morphological Modelling of a Random Fibrous Network.* Image Analysis and Stereology, 2009. **28**: p. 129-141.
30. Hansen, J.C., et al., *An elastic network model based on the structure of the red blood cell membrane skeleton.* Biophysical Journal, 1996. **70**(1): p. 146-166.
31. Kim, Y.A., et al., *Fabrication of high-purity, double-walled carbon nanotube buckypaper.* Chemical Vapor Deposition, 2006. **12**(6): p. 327 - 330.
32. Yao, Y.T., A. Alderson, and K.L. Alderson, *Can nanotubes display auxetic behaviour?* Physica Status Solidi B-Basic Solid State Physics, 2008. **245**(11): p. 2373-2382.
33. Coluci, V.R., et al., *Modeling the auxetic transition for carbon nanotube sheets.* Physical Review B, 2008. **78**(11).
34. Kukovecz, A., et al., *Controlling the pore diameter distribution of multi-wall carbon nanotube buckypapers.* Carbon, 2007. **45**(8): p. 1696-1698.
35. Das, R.N., et al., *Engineered Macroporosity in Single-Wall Carbon Nanotube Films.* Nano Letters, 2009. **9**(2): p. 677-683.
36. Whitby, R.L.D., et al., *Geometric control and tuneable pore size distribution of buckypaper and buckydiscs.* Carbon, 2008. **46**(6): p. 949-956.
37. Kusworo, T.D., et al., *CO_2 Removal from Biogas Using Carbon Nanotubes Mixed Matrix Membranes.* International Journal of Engineering Science, 2010. **1**(1): p. 1-6.
38. Srivastava, A., et al., *Carbon nanotube filters.* Nature Materials, 2004. **3**(9): p. 610-614.
39. Kang, S., et al., *Single-walled carbon nanotubes exhibit strong antimicrobial activity.* Langmuir, 2007. **23**(17): p. 8670-8673.
40. Song, C.S., et al., *Controllable Synthesis of Single-Walled Carbon Nanotube Framework Membranes and Capsules.* Nano Letters, 2009. **9**(12): p. 4279-4284.
41. Pharr, G.M., W.C. Oliver, and F.R. Brotzen, *On the Generality of the Relationship among Contact Stiffness, Contact Area, and Elastic-Modulus during Indentation.* Journal of Materials Research, 1992. **7**(3): p. 613-617.
42. Hall, L.J., et al., *Sign change of Poisson's ratio for carbon nanotube sheets.* Science, 2008. **320**(5875): p. 504-507.
43. Coleman, J.N., et al., *Improving the mechanical properties of single-walled carbon nanotube sheets by intercalation of polymeric adhesives.* Applied Physics Letters, 2003. **82**(11): p. 1682-1684.
44. Barrera, E.V., *Key methods for developing single-wall nanotube composites.* Jom-Journal of the Minerals Metals & Materials Society, 2000. **52**(11): p. A38-A42.

45. Ramanathan, T., et al., *Amino-functionalized carbon nanotubes for binding to polymers and biological systems.* Chemistry of Materials, 2005. **17**(6): p. 1290-1295.
46. Li, D. and Y.N. Xia, *Electrospinning of nanofibers: Reinventing the wheel?* Advanced Materials, 2004. **16**(14): p. 1151-1170.
47. Huang, Z.M., et al., *A review on polymer nanofibers by electrospinning and their applications in nanocomposites.* Composites Science and Technology, 2003. **63**(15): p. 2223-2253.
48. Yang, F., et al., *Electrospinning of nano/micro scale poly(L-lactic acid) aligned fibers and their potential in neural tissue engineering.* Biomaterials, 2005. **26**(15): p. 2603-2610.
49. Knowles, T.P., et al., *Nanostructured biofilms from hierarchical self-assembly of amyloidogenic proteins.* Nature Nanotechnology, 2010. **5**(3): p. 204 - 207
50. Humphrey, W., A. Dalke, and K. Schulten, *VMD: Visual molecular dynamics.* Journal of Molecular Graphics, 1996. **14**(1): p. 33-38.

TABLE(S) AND TABLE CAPTIONS

Table 1

Summary of mesoscopic parameters derived for (5,5) SWCNTs [14] and (8,8)-(12,12) DWCNTs [14, 16]

Parameter	Units	(5,5) SWCNT	(8,8)-(12,12) DWCNT
Equilibrium bead distance r_0	Å	10	10
Tensile stiffness, k_t	kcal/mol/Å^2	1000	3760
Equilibrium angle, θ_0	degrees	180	180
Bending stiffness, k_B	kcal/mol/Å^2	14,300	180,000
Dispersive parameter, ε	kcal/mol	15.10	21.6
Dispersive parameter, σ	Å	9.35	19.70

Table 2

(a) Porosity due to variation of initial nanotube density (spacing); SWCNT only

Initial Nanotube Spacing Å	Porosity Ω
10	0.473
25	0.576
50	0.771
75	0.858
100	0.902

(b) Porosity due to variation of DWCNT content (percentage by weight)

DWCNT Content	Porosity Ω
0%	0.473
16%	0.424
30%	0.303
50%	0.283

Table 3

Summary of nanoindentation simulation results based on variations of the buckypaper porosity

Porosity	Contact Stiffness (N/m)	Modulus (GPa)
Variable SWCNT density		
0.902	3.8	0.22
0.858	8.7	0.50
0.771	9.2	0.53
0.576	22.9	1.33
0.473	24.4	1.41
Variable DWCNT content		
0.473	24.4	1.41
0.424	32.0	1.85
0.303	33.5	2.74
0.283	59.7	3.14

FIGURES AND FIGURE CAPTIONS

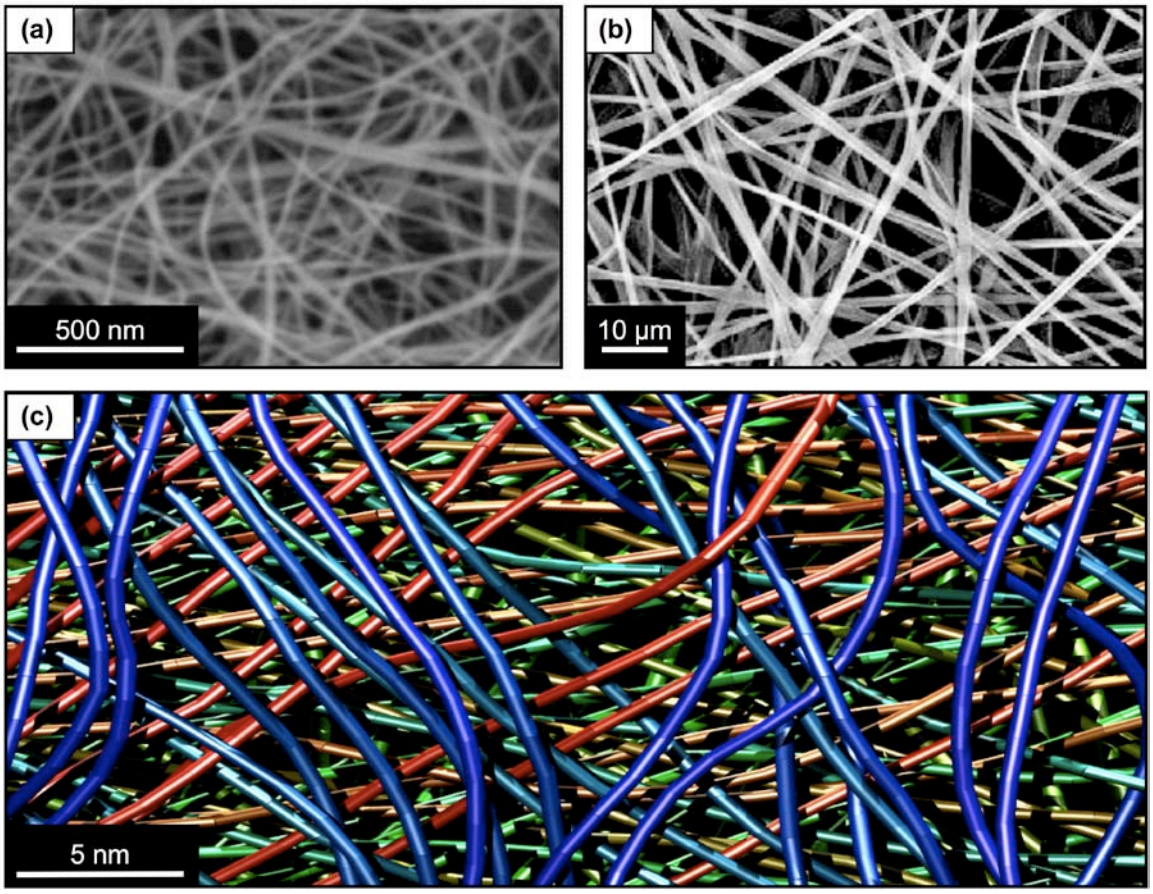

Figure 1: Comparison between experiment and simulation. Synthesized examples of entangled fibrous systems including (a) buckypaper and (b) electrospun polymer fibers; (c) developed mesoscale model of entangled carbon nanotubes via *in silico* assembly procedure (colors added to accentuate individual tubes and layers). [(a) from [7], open access reproduction permitted (doi:10.3390/ma3010127); (b) from [48], reproduced with permission from *Biomaterials*, copyright © 2005, Elsevier Ltd.).

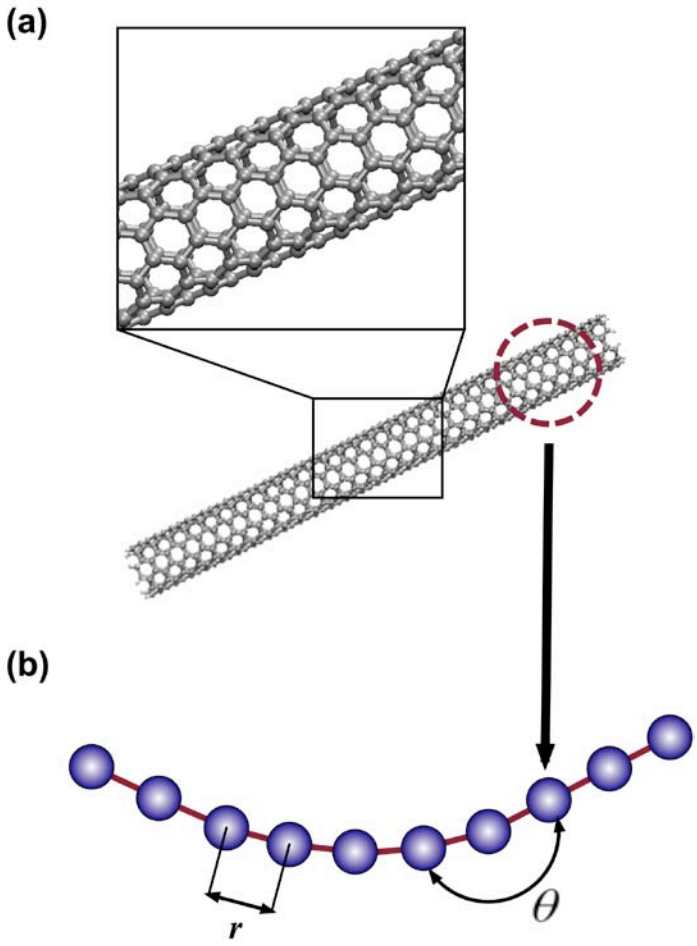

Figure 2: Coarse-grain representation of carbon nanotube through “fine-trains-coarse” approach: (a) Full atomistic and corresponding (b) mesoscopic bead-spring model of a carbon nanotube. Parameters for tensile, bending, and pair potentials of (5,5) SWCNT and (8,8)-(12,12) DWCNT given in Table 1.

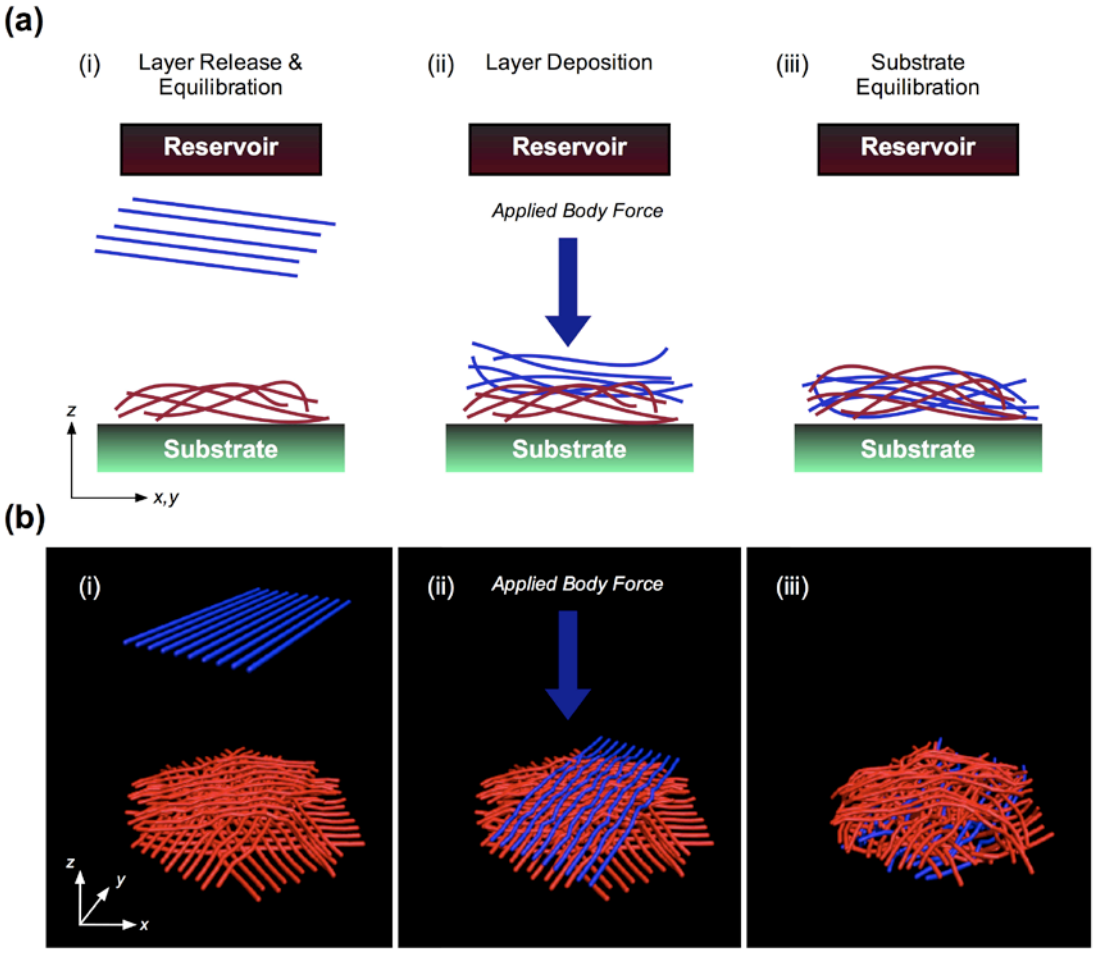

Figure 3: *In silico* assembly of buckypaper representation. (a) Schematic figures and (b) simulation snapshots of primary steps of buckypaper assembly procedure: (i) Nanotube layer released from reservoir (fixity removed) and equilibrated at constant temperature; (ii) deposition through applied body force to previously accumulated nanotube layers, reduction in pair wise interactions and bending stiffness facilitate entanglement and disorder; (iii) body force removed and new nanotube agglomeration equilibrated. The process is repeated for succeeding layers, after which the reduced parameters (k_θ and ε) are increased to their full values. Coloring added to distinguish deposited layer (blue) to previously entangled structure (red).

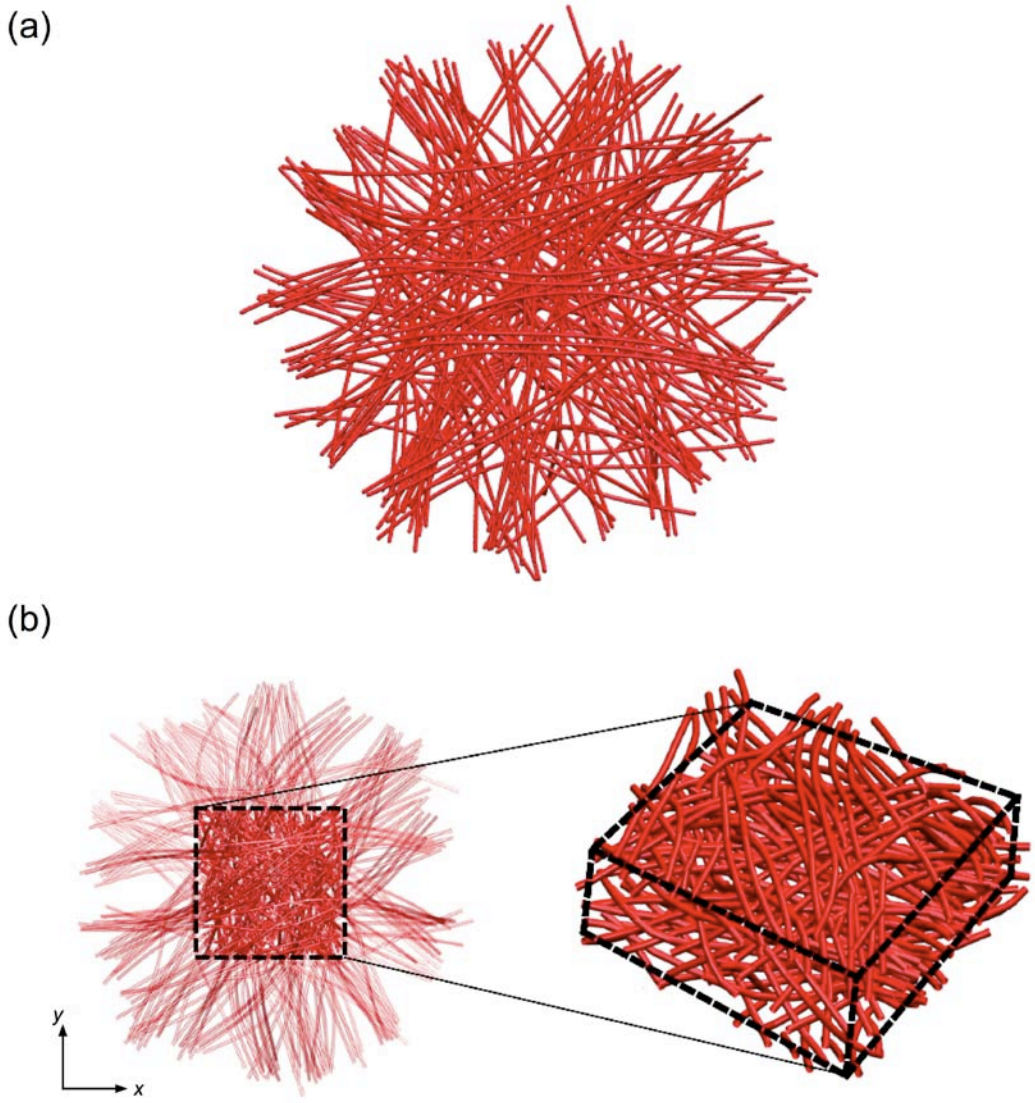

Figure 4: Example buckypaper model and representative volumetric element (RVE). (a) As assembled representative buckypaper model; twelve layers, consisting of ten individual nanotubes (120 nanotubes total) of constant length (50 nm). During assembly, each layer is rotated thirty degrees about a central axis, such that 12 layers represent a complete 360° period of initial tube orientation to maintain material isotropy. (b) Schematic of selected RVE of buckypaper model, consisting of a central interior region of 200 Å x 200 Å x 100 Å, used for porosity characterization.

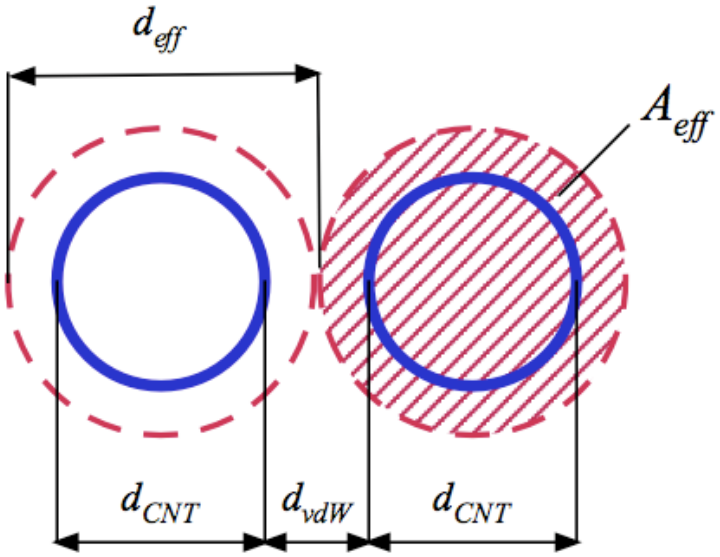

Figure 5: Assumed cross-sectional area of nanotubes for porosity calculation, were the effective diameter (d_{eff}) considers the nanotube diameter (d_{CNT}) plus the van der Waals spacing (d_{vdW}).

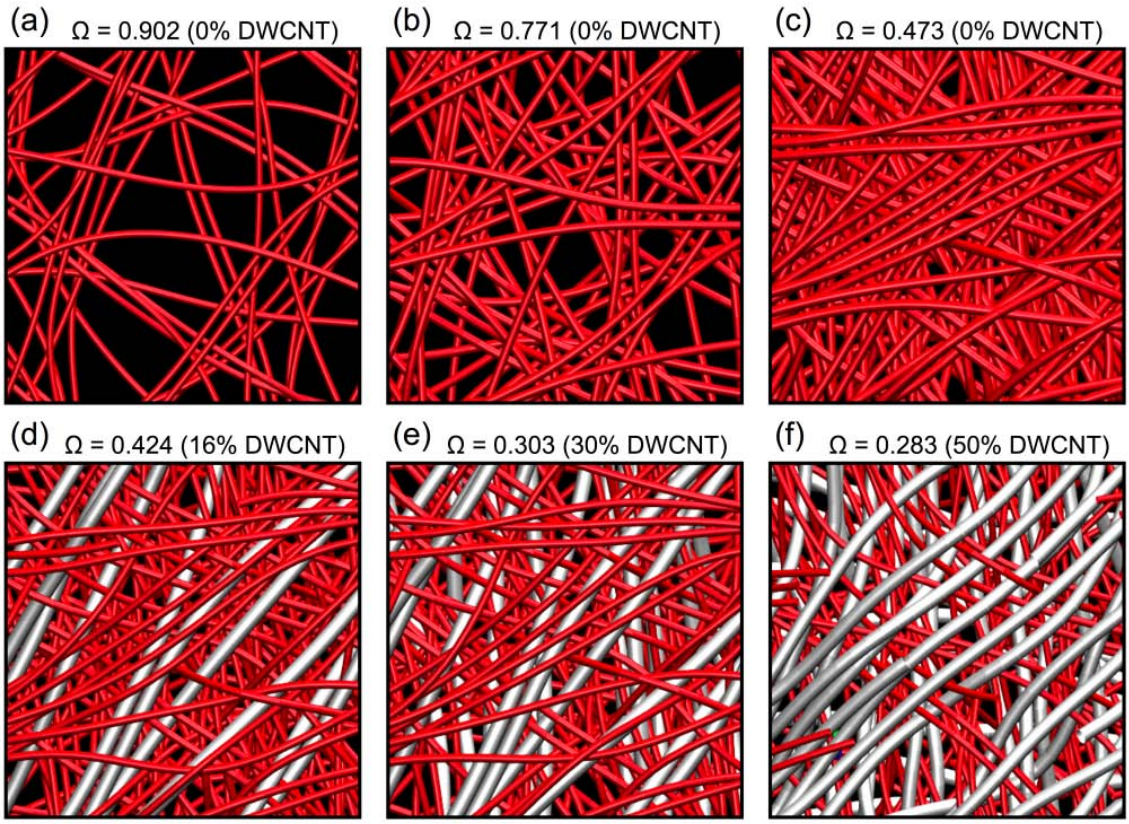

Figure 6: Representative visualizations of RVE of buckypaper model with variation of porosity. (a) to (c) variation of porosity due to initial SWCNT density; (d) to (f) variation of porosity due to increase of DWCNT content (SWCNTs in red; DWCNTs in white).

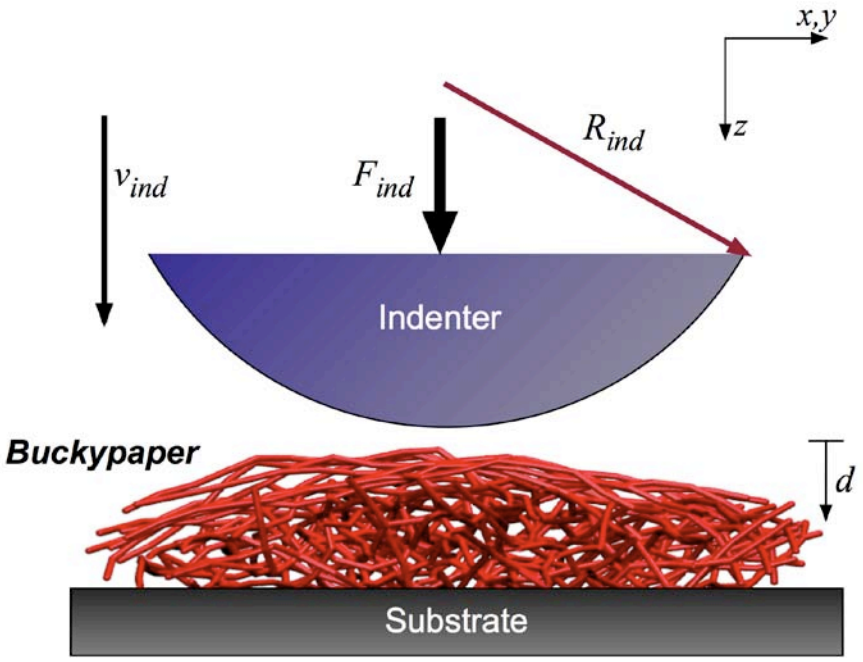

Figure 7: Schematic of nanoindentation of buckypaper model. Indention parameters include an indenter radius of 20 nm, speed of 30 m/s, and a force constant (*K*) of 10 N/m (Eq. (7)). Indentation depth measured from initial contact point, and limited to 2.0 nm to permit small deformation assumption. Indentation force (nN) and indentation depth (nm) recorded for each simulation.

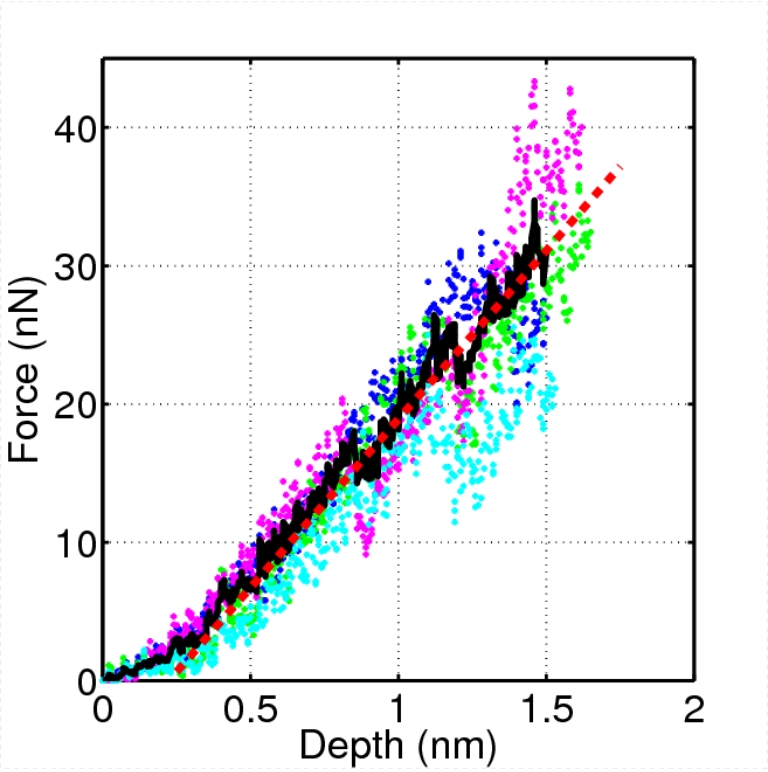

Figure 8: Representative nanoindentation force v. indentation depth results for model of all (5,5) SWCNTs, porosity 0.473. Results depicted for four separated indentation runs, with average shown as solid line and linear regression fitting shown as dashed line. Resulting contact stiffness of approximately 24.4 N/m, resulting in a Young's modulus of approximately 1.41 GPa (by Eq. (8) through Eq. (10)). Table 3 summarizes results for all buckypaper configurations.

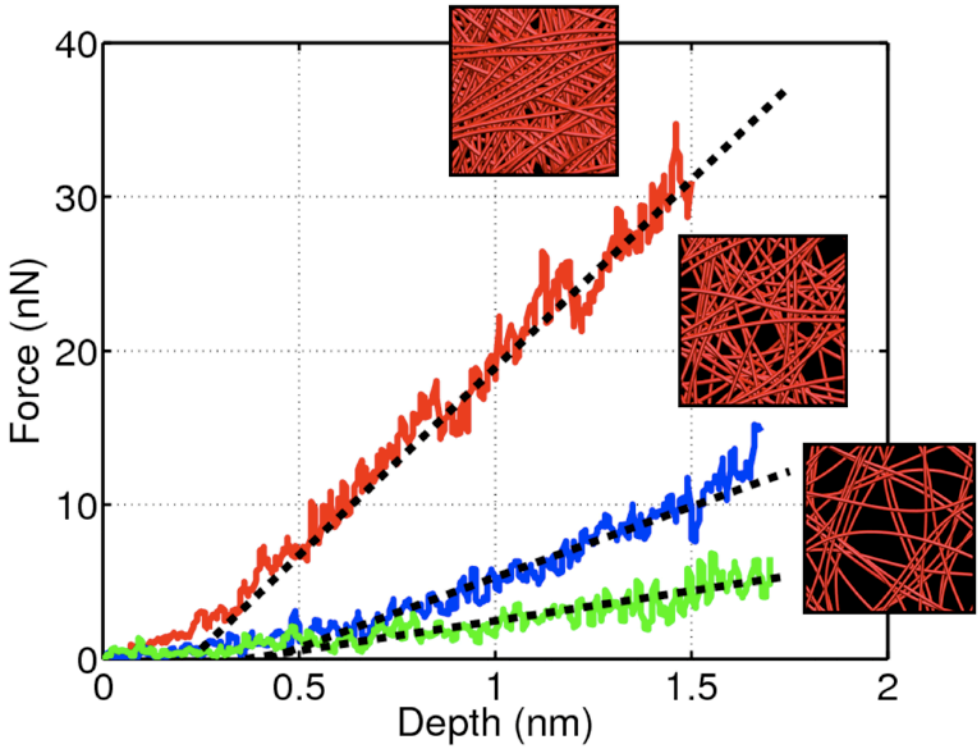

Figure 9: Average nanoindentation force versus depth for SWCNT only configurations of representative porosities 0.473, 0.771, and 0.902 (intermediate results omitted for clarity). Results correspond to Young's modulii of 1.41 GPa, 0.53 GPa, and 0.22 GPa respectively (Eq. (8) through (10)). Average of four indentation simulations calculated, with linear regression taken from indentation depth of 0.5 to 1.5 nm.

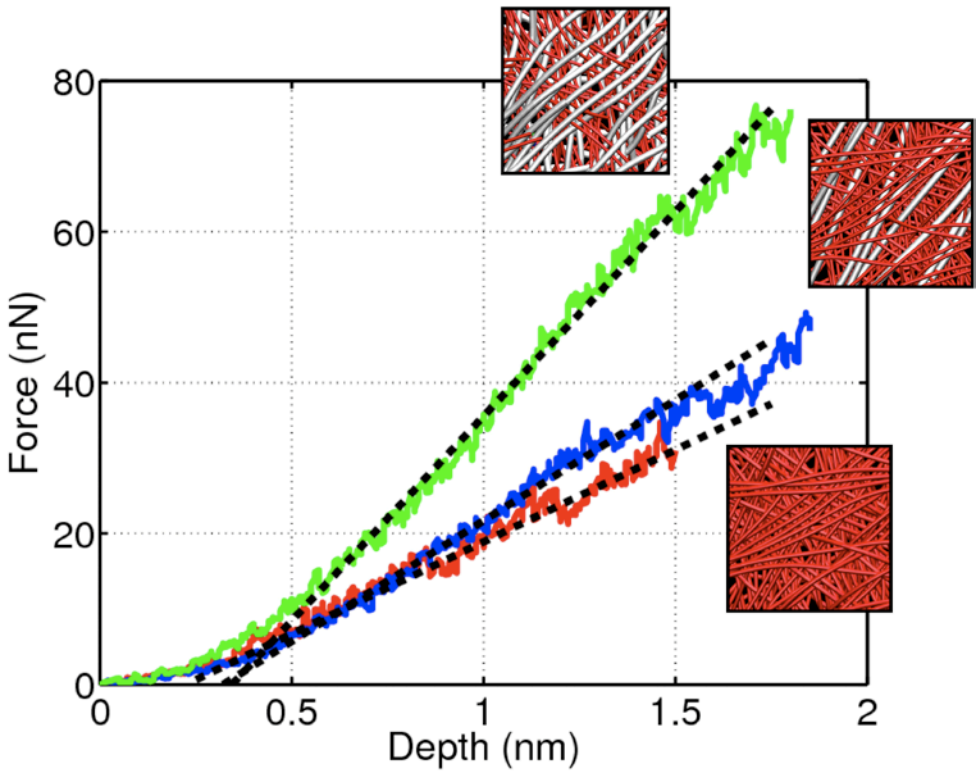

Figure 10: Average nanoindentation force versus depth for SWCNT + DWCNT configurations of representative DWCNT content 50%, 16%, and 0% by weight (intermediate results omitted for clarity). Results correspond to Young's moduli of 3.14 GPa, 1.85 GPa, and 1.41 GPa respectively (Eq. (8) through (10)). Noted that 0% DWCNT content is the same model configuration as 0.473 porosity as depicted in Figure 10. Average of four indentation simulations calculated, with linear regression taken from indentation depth of 0.5 to 1.5 nm.

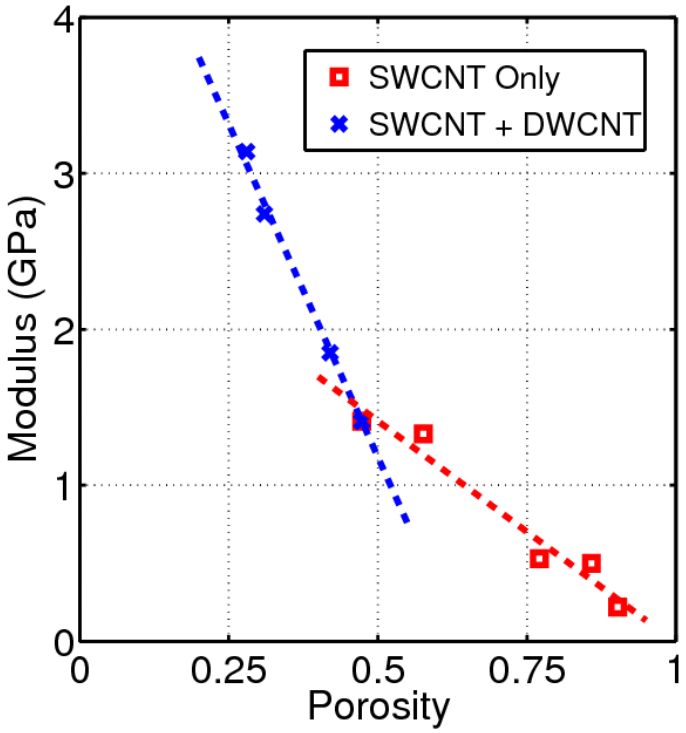

Figure 11: Trends in modulus variation as a function in porosity for model configurations of SWCNT (red squares) and SWCNT + DWCNT configurations (blue crosses). Decrease in modulus attributed less constituent nanotubes for SWCNT only models, while increase in modulus attributed to increase in larger diameter, stiffer elements in SWCNT + DWCNT models.